Journal of Inorganic Biochemistry 240 (2023) 112096

Contents lists available at ScienceDirect

Journal of Inorganic Biochemistry

journal homepage: www.elsevier.com/locate/jinorgbio

Incorporation of a molybdenum atom in a Rubredoxin-type Centre of a *de novo*-designed α_3DIV-L21C three-helical bundle peptide

Pedro M.S. Bragança [a,b,c], Marta S.P. Carepo [a,d,*], Sofia R. Pauleta [b,c], Tyler B.J. Pinter [e], Maddalena Elia [a], Cristina M. Cordas [a], Isabel Moura [a], Vincent L. Pecoraro [e], José J.G. Moura [a,*]

[a] LAQV, REQUIMTE, Department of Chemistry, NOVA School of Science and Technology, Universidade NOVA de Lisboa, 2829-516 Caparica, Portugal
[b] Microbial Stress Lab, UCIBIO – Applied Molecular Biosciences Unit, Department of Chemistry, NOVA School of Science and Technology, Universidade NOVA de Lisboa, 2829-516 Caparica, Portugal
[c] Associate Laboratory i4HB - Institute for Health and Bioeconomy, NOVA School of Science and Technology, Universidade NOVA de Lisboa, 2829-516 Caparica, Portugal
[d] Escola de Psicologia e Ciências da Vida, Departamento de Ciências da Vida, Universidade Lusófona de Humanidades e Tecnologias, Campo Grande, 1749-024 Lisboa, Portugal
[e] Department of Chemistry and Biophysics, University of Michigan, Ann Arbor, MI 48109-1055, United States

ARTICLE INFO

Keywords:
A de novo protein design
Three-helix bundle
Molybdenum
Models of molybdenum-containing enzymes
Rubredoxin
Tetracysteinyl coordination

ABSTRACT

The rational design and functionalization of small, simple, and stable peptides scaffolds is an attractive avenue to mimic catalytic metal-centres of complex proteins, relevant for the design of metalloenzymes with environmental, biotechnological and health impacts. The *de novo* designed α_3DIV-L21C framework has a rubredoxin-like metal binding site and was used in this work to incorporate a Mo-atom. Thermostability studies using differential scanning calorimetry showed an increase of 4 °C in the melting temperature of the Mo-α_3DIV-L21C when compared to the apo-α_3DIV-L21C. Circular dichroism in the visible and far-UV regions corroborated these results showing that Mo incorporation provides stability to the peptide even though there were almost no differences observed in the secondary structure. A formal reduction potential of ~ −408 mV *vs.* NHE, pH 7.6 was determined. Combining electrochemical results, EPR and UV–visible data we discuss the oxidation state of the molybdenum centre in Mo-α_3DIV-L21C and propose that is mainly in a Mo (VI) oxidation state.

1. Introduction

The field of rational protein design has been increasing significantly in the areas of fundamental research (biochemistry and biotechnology), clinical applications and applied (industrial) areas, with relevance in the topics of added value products and energy [1,2]. The underlying ambition is to enhance native protein's performances or to create new scaffolds, in order to better understand protein structure-function relationships and, ultimately, to develop artificial enzymes with higher efficiencies and selectivities [3–5]. To design such artificial enzymes two approaches have been employed: the protein redesign, using native proteins scaffolds as model templates, and *a de novo* protein design, by the creation of peptide scaffolds from scratch. Both methods are important from a coordination and biochemistry point-of-view and for the mimicking of crucial metalloenzymes [6–9].

A de novo metalloprotein design aims to develop efficient catalysts that perform biological functions with the same selectivity and high efficiency as the native counterparts, under mild conditions. The construction of novel metal-binding sites in designed scaffolds can also unravel the structural and catalytic roles imposed by the metal ions in native systems [10–12]. To design such stable native-like frameworks from scratch, the approach exploits fundamental amino acid

Abbreviations: EPR, Electron Paramagnetic Resonance; NHE, normal hydrogen reference electrode (equivalent to SHE, standard hydrogen reference electrode); DMSOR, dimethyl sulfoxide reductase; MGD, bis-molybdopterin guanine dinucleotide; NMR, (Nuclear Magnetic Resonance); TTM, Ammonium tetrathiomolybdate; TCEP, 3,3′,3′′-phosphanetriyltripropanoic acid; DMF, dimethylformamide; DTT, dithiothreitol; ICP-AES, Inductively Coupled Plasma–Atomic Emission Spectroscopy; BSA, Bovine Serum Albumin; CD, (Circular Dichroism); DSC, Differential scanning calorimetry; PG, Pyrolytic Graphite; SCE, Saturated Calomel Electrode; EXAFS, Extended X-ray absorption fine structure.

* Corresponding authors at: LAQV, REQUIMTE, Department of Chemistry, NOVA School of Science and Technology, Universidade NOVA de Lisboa, 2829-516 Caparica, Portugal.

E-mail addresses: marta.carepo@fct.unl.pt (M.S.P. Carepo), jose.moura@fct.unl.pt (J.J.G. Moura).

https://doi.org/10.1016/j.jinorgbio.2022.112096
Received 29 September 2022; Received in revised form 17 November 2022; Accepted 4 December 2022
Available online 22 December 2022

interactions that contribute to the folding and topology of the protein constructs, such as hydrophobic and van der Waals contacts, hydrogen bonding, and salt-bridges [13,14].

Iron-sulfur proteins are one of the earliest, ubiquitous, abundant, and functionally relevant metalloredox proteins found in all living organisms [15]. This collection includes a broad array of structures, from simple mononuclear proteins, such as rubredoxins and ferredoxins, to large heteronuclear and mixed clusters. The simple 1-Fe centre rubredoxin is an important model metalloprotein used for the protein redesign approach and, more recently, for *a de novo* protein design. Such proclivity relies on the fact that rubredoxin is one of the simplest and smaller iron-sulfur bacterial proteins (≈6 kDa) in which the single Fe ion is coordinated by four sulfur atoms of four cysteine residues, $Fe(S\text{-}Cys)_4$, arranged in a distorted tetrahedral environment [16,17]. This cysteinyl coordination environment provides a sulfur-rich first coordination sphere similar to other sulfur-rich metal-binding sites, such as bacterial [NiFe] hydrogenase [18,19], Cu-chaperones [20,21], and molybdenum-containing proteins [22].

Until now, several studies in protein redesign were able to exploit the tetra-cysteinyl metal coordination site of rubredoxin to incorporate a wide variety of metal ions and, ultimately, develop bio-models and spectroscopic probes [22–29]. The Mo in the Mo-rubredoxin substituted protein is coordinated by four thiol groups from the four conserved cysteines and by two exogenous ligands, an oxygen atom and another ligand that can be either a -OH or a SR [30]. The Mo is in the $Mo^{(VI)}$ oxidation state and can be reduced to $Mo^{(IV)}$ with sodium dithionite. The Mo-rubredoxin was considered a suitable model for the dimethylsulfoxide reductase (DMSOR) Mo bis-MGD (bis-molybdopterin guanine dinucleotide) family, which features a Mo atom coordinated with four sulfur atoms, from two pyranopterin guanosine dinucleotide, in a trigonal prismatic geometry ($[Mo^{(VI)}O(MPT)_2(X)]$ [31].

The first reported example of *a de novo* design scaffold with a rubredoxin-like active-site in a novel and unrelated native fold was the synthetic peptide α_3DIV-L21C [32,33]. This construct was obtained through the functionalization of a three-helix bundle scaffold – α_3DIV, with the creation of a tetrathiolate metal-binding site [34].

The apo-α_3DIV-L21C scaffold was anaerobically reconstituted with ferrous iron forming a Fe-α_3DIV-L21C peptide that was able to mimic some spectroscopic properties of native rubredoxin, such as the UV–visible, Mössbauer, electron paramagnetic resonance (EPR) and magnetic circular dichroism spectra, as well as its formal reduction potential [32]. These results pointed out that the overall protein fold is not crucial for the spectroscopic properties observed for rubredoxin. Thus, the type of ligands and their spatial coordination in the metal site of rubredoxin is more relevant for these spectroscopic and electrochemical properties compared with specific folding features. The incorporation of different biologically active metals into an α_3DIV-L21C general scaffold could tune these sites for alternative natural and non-natural functions. As an example, placing Cd(II) into rubredoxin yields a UV chromophore with bands at 213, 229 and 245 nm [35] and a signal at 734 ppm from ^{113}Cd NMR (nuclear magnetic ressonance) [36], whereas Cd(II) α_3DIV-L21C has corresponding features at 224 and 243 nm and 685 ppm [37]. These data supported the assignment that Cd(II) lead to a well formed, tetrahedral CdS_4 environment in rubredoxin, however, the α_3DIV-L21C was best described as a mixture of CdS_4 and CdS_3O centers [37]. This comparison suggested that a larger metal was not as well accommodated in the designed helical bundle as compared to the native rubredoxin fold. To this date, studies of alternative redox active metals with α_3DIV-L21C to test the design parameters of this site have not been reported. Therefore, this paper focuses on the incorporation of a molybdenum atom within the rubredoxin-type metal-binding site of *a de novo*-designed three-helix bundle peptide – α_3DIV-L21C to assess how broadly the design can mimic the chemistry of Mo rubredoxin. The spectroscopic, thermodynamic, and electrochemical properties of the Mo-α_3DIV-L21C are examined, the favoured Mo oxidation state is identified, and explanations provided to address the observed differences with Mo rubredoxin.

2. Materials methods

2.1. α_3DIV-L21C production and purification

The construct α_3DIV-L21C was generated by sequential site-directed mutagenesis and the production, purification and lyophilization were done as previously described [32]. The calculated molecular mass of the purified peptide is 8209 $g.mol^{-1}$ and the molar extinction coefficient of the apo-form at 280 nm is 8460 M^{-1} cm^{-1}.

2.2. Modelling the α_3DIV-L21C scaffold

The three-dimensional structure of the apo-α_3DIV-L21C peptide with the tetracysteinyl environment, as the metal-binding site, was obtained through homology modelling using the SWISS MODEL Workspace from ExPASy – SIB Bioinformatics Resource Portal. The input target was "GSWAEFKQRLAAIKTRCQACGGSEAECAAFEKEIAAFE-SELQAYKGKGNPEVEAL.

RKEAAAIRDECQAYRHN", and the coordinates used as a template for modelling were 2MTQ, which corresponds to the apo-α_3DIV synthetic peptide [38]. Energy minimization was performed in the program Chimera 1.11 [39].

2.3. Insertion of molybdenum in the α_3DIV-L21C peptide and absorption spectroscopy

Ammonium tetrathiomolybdate (TTM) compound was used as the Mo source to obtain the Mo-α_3DIV-L21C peptide. The reconstitution procedure started with the preparation of a 250 μM solution of apo-α_3DIV-L21C in 50 mM Tris-HCl pH 7.6, containing 500 μM of 3,3′,3″-phosphanetriyltripropanoic acid (TCEP). A 10 mM TTM solution was prepared in 50 mM Tris-HCl pH 7.6, containing 20% (*V*/V) *N*, *N*-dimethylformamide (DMF). To optimize the Mo incorporation procedure different peptide:metal ratios: 1:1, 1:4, 1:6, 1:8, 1:9, 1:10 and 1:15 were tested at room temperature and 50 °C for 2 h. Afterwards, the samples were centrifuged for 10 min at 4500*g* and loaded into a Sephadex™ G-25 PD-10 desalting column, (Cytiva), equilibrated with 50 mM Tris-HCl pH 7.6 to remove the unbound metal. The UV–visible spectra of the peptide were recorded on a Shimadzu UV-1800 spectrophotometer. The reconstitution procedure described above was performed under aerobic and anaerobic conditions (MBraun UNIlab anaerobic chamber). The incubation with dithiothreitol (DTT) or sodium dithionite were performed with 0.4 and 0.2 equivalents respectively, under anaerobic conditions to reduce the sample but simultaneously avoiding the overlap of the peptide signal with the signal of DTT and dithionite at 320 nm.

2.4. Metal and protein quantification

Mo was quantified by Inductively Coupled Plasma – Atomic Emission Spectroscopy (ICP-AES), in an ICP Horiba Jobin-Yvon (Ultima) spectrometer, using the standard solution Reagecon 23 multi-elements in a concentration range between 0.05 and 3 ppm. Total protein was quantified by the colorimetric Lowry Method [40], using bovine serum albumin (BSA) as a standard protein.

2.5. Circular dichroism spectroscopy

Circular dichroism (CD) spectra were recorded in an Applied Photophysics Chirascan™ qCD spectrometer. The CD data were either reported in millidegrees (mdeg) of ellipticity (θ) as a function of wavelength or represented in mean residue ellipticity ($[\theta]_{MRE}$) as a function of wavelength [41–43]. The $[\theta]_{MRE}$ is the CD raw data corrected for the peptide concentration using the following eq. 1.

$$[\theta]_{MRE} = \frac{\theta(deg) \times MRW}{10 \times L \times C} \quad (1)$$

in which MRW (Mean Residue Weight) represents the molecular mass of the peptide divided by N-1 (with N being the number of residues), C represents the concentration of protein ($g.mL^{-1}$) and L is the cell path length (cm).

For the far-UV studies (190–260 nm) 15 μM apo- and 11 μM Mo-peptide forms were prepared in 10 mM Tris-HCl pH 7.6 buffer with 0.5 mM of TCEP. The measurements were performed in a 1 mm path length cuvette with a total volume of 300 μL. The CD spectra presented are an average of three spectral acquisitions at 25 °C, before and after the temperature cycle, with bandwidth and a step-size of 1 nm. The temperature-dependent far-UV CD spectra were recorded in a temperature range of 10 °C to 94 °C, with a stepped ramp mode of 0.4 s per point, a temperature increment of 2 °C for each measurement and a stabilization period of 1 min between each point.

Furthermore, information about the tertiary structure fingerprint [44] and metal-ligand interactions (L → M charge-transfer transitions or metal d–d transitions) were also studied, exclusively, for the Mo-α_3DIV-L21C form. These data were obtained by studying the near-UV region (260–320 nm) and the visible region (320–600 nm) [45]. For these studies, a sample of Mo-peptide form, with a concentration of 70 μM, was prepared in 10 mM Tris-HCl pH 7.6 buffer with 0.5 mM of TCEP. The measurements were performed in a 10 mm path length quartz cuvette with a total volume of 2 mL. The CD spectra presented are an average of three spectral acquisitions at 25 °C, before and after the temperature ramp, with bandwidth and a step-size of 1 nm. The temperature-dependent near-UV/visible CD spectra were performed in a temperature range of 19 °C to 94 °C, with a stepped ramp mode of 0.3 s per point, a temperature increment of 3 °C, and a stabilization period of 2 min between each point.

The change in the mean residue ellipticity as a function of temperature was fitted to estimate the apo- and Mo-peptide's thermodynamic parameters, such as the melting temperature (T_m) and the enthalpy of unfolding (ΔH), for the far-UV and visible regions [46].

2.6. Differential scanning calorimetry (DSC)

Differential scanning calorimetry was performed in a TA™ Nano DSC apparatus. The thermodynamic parameters and melting temperature were obtained by fitting the thermograms in a NanoAnalyze™ v3.10.0 Data Analysis software (TA Instruments).

The samples of apo- and Mo-peptides were prepared in 50 mM phosphate buffer at pH 7.6 with 0.1 mM of TCEP. The protein concentrations were 0.36 $mg.mL^{-1}$ and 0.47 $mg.mL^{-1}$ for the Mo- and apo-peptide, respectively. The temperature range used in the experiments was from 20 °C to 95 °C.

2.7. Electrochemical characterization

The electrochemical behaviour, of the apo- and Mo-α_3DIV-L21C systems, was studied with an AUTOLAB Potentiostat/Galvanostat Type III, using one compartment electrochemical cell, in a three-electrode configuration. The data acquisition was performed using GPES software. Working, secondary and reference electrodes were pyrolytic graphite (PG), a Pt wire and a saturated calomel electrode (SCE), respectively. The potentials were converted and are presented in the normal hydrogen electrode (NHE) reference scale. The target electroactive species were immobilized using a membrane (spectra/Por, cut-off 3.5 kDa), in a thin layer configuration [47–49]. The preparation and assays were attained in strict anaerobic environment (inside a MBraun UNIlab anaerobic chamber). Before each experiment, the PG electrode was polished with 0.3 and 1 μm alumina suspension (BUEHLER), cleansed with deionized water, immersed in an ultra-sound bath for 3 min and lastly again thoroughly cleaned with deionized water. For each experiment, 15 μL of apo-α_3DIV-L21C (200–250 μM) or 15 μL Mo-α_3DIV-L21C (50–150 μM) were placed on the PG surface. To enhance the electrochemical signal, 4 μL of a neomycin sulphate solution (2 mM) (Sigma Aldrich) was also added to the working electrode surface together with the peptide solution drop. Solvent casting technique was applied, at room temperature, until the mixed solution on the surface decreased the initial volume, and then the membrane was applied, entrapping the target species. The controls have shown that neomycin sulphate does not present any electrochemical process in the applied experimental conditions neither interacts with the peptide, being its role to enhance the electrostatic interaction between the electrode and the peptide. The electrolyte solution (25 mL) consisted of 50 mM Tris-HCl, pH 7.6, 100 mM of NaCl, 2 mM neomycin sulphate and 500 μM TCEP. Several scan rates, from 5 mVs^{-1} to 100 mVs^{-1}, were tested. All the solutions were degassed with a continuous flow of argon, for at least 30 min, before being introduced into the anaerobic chamber.

2.8. Electron paramagnetic resonance of the Mo-α_3DIV-L21C peptide

EPR spectroscopy was done using a Bruker EMX spectrometer equipped with an Oxford Instruments ESR-900 continuous-flow helium cryostat and a high-sensitivity perpendicular mode rectangular cavity. The Mo-α_3DIV-L21C peptide had a final concentration of 400 μM and the spectra were acquired at 77 K. The peptide was incubated inside an anaerobic chamber (MBraun UNIlab) with sodium dithionite (5 mM, ~10 times more concentrated) and the EPR spectra were collected immediately after reduction and after 15 and 30 min incubations.

3. Results

3.1. Molybdenum reconstitution and UV–vis characterization

The incorporation of Mo in the apo-α_3DIV-L21C peptide was performed under reducing conditions to prevent the formation of disulphide bonds and to enhance the metal incorporation. Several peptide/metal ratios were tested (1:1, 1:4, 1:6, 1:8, 1:9, 1:10 and 1:15) at two different temperatures (20 and 50 °C), under aerobic and anaerobic conditions. Neither the temperature nor the presence of oxygen influenced the Mo incorporation. A ratio of 1 peptide: 1 Mo was obtained when the peptide was incubated with TTM in a 1 peptide: 9 Mo molar ratio for 2 h at room temperature followed by size exclusion chromatography to remove unbound metal. Metal and protein quantification data revealed a 90% occupancy, with the protein solution having a yellow-white colour.

In Fig. 1 is represented the UV–visible spectrum of Mo-α_3DIV-L21C obtained under aerobic conditions at room temperature. The Mo peptide has two unresolved shoulders at 320 nm ($\varepsilon = 7400\ M^{-1}.cm^{-1}$) and 460 nm ($\varepsilon = 2000\ M^{-1}.cm^{-1}$), characteristic of thiolate-Mo charge-transfer bands. The TTM compound, used to reconstitute the apo-α_3DIV-L21C, has two well-defined bands with absorption maxima at 318 and 469 nm (Fig. 1-inset). The broadening of the bands together with the wavelength shift of the absorption maxima observed in the UV–visible absorption spectrum of Mo-α_3DIV-L21C compared to TTM suggests the incorporation of Mo in the tetracysteinyl environment of the α_3DIV-L21C.

3.2. Circular dichroism characterization

CD studies in the far-UV region (190–260 nm), provide information about the topology and the content of the peptide's secondary structure. The far-UV CD spectra for both apo-α_3DIV-L21C and Mo-α_3DIV-L21C forms confirm the helical conformation of the α_3DIV-L21C scaffold (Fig. S1). The $[\Theta]_{222}/[\Theta]_{208}$ ratios at 25 °C for both forms of the peptide in the presence or absence of a reducing agent (TCEP) are presented in Table 1. The $[\Theta]_{222}/[\Theta]_{208}$ ratios are 1 and 0.98 for apo- and Mo- α_3DIV-L21C, respectively, supporting the proposal that incorporation of one molybdenum atom within the metal-binding site does not significantly

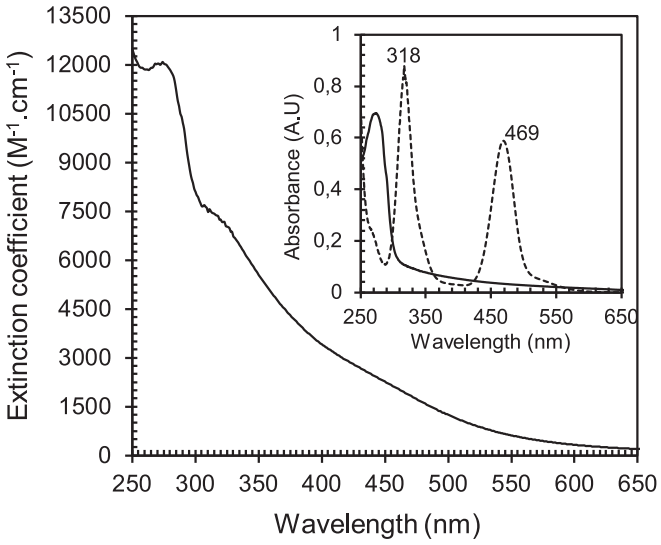

Fig. 1. Mo-α_3DIV-L21C UV–visible spectrum in 50 mM Tris-HCl pH 7.6. Inset: Spectra of apo-α_3DIV-L21C (black line) and TTM (dashed line).

affect the secondary structure profile, although Mo binding may cause a slight decrease in the helicity. This is observed regardless of the presence of TCEP in the sample buffer (Table 1).

The thermal stability of apo- and Mo-α_3DIV-L21C was also accessed by CD (Fig. 2). The melting temperature (T_m) and the enthalpy of folding (ΔH) for both apo- and Mo-α_3DIV-L21C forms, in the presence of TCEP, were obtained by fitting the experimental data to a two-state transition model of a monomer from a folded to an unfolded state that assumes an equal heat capacity for both states ($\Delta Cp = 0$) [46].

The melting temperature estimated for both apo- and Mo-α_3DIV-L21C (in the presence of TCEP), is the same, 60.2 °C. Furthermore, the enthalpy of unfolding (ΔH) was also estimated for both peptide forms, being 112.6 kJ.mol^{-1} and 90.1 kJ.mol^{-1} for the apo- and the Mo-α_3DIV-L21C, respectively.

The CD spectrum of Mo-α_3DIV-L21C in the visible region, in the presence of TCEP, exhibits an intense positive absorption band with a maximum at 392 nm (Fig. 3A-black line), which is also observed in the absence of TCEP (Fig. 3D), whereas the TTM solution used in the reconstitution assays has no CD signal (Fig. 3A- dashed line).

The thermal stability in the visible region was also evaluated. The variation in mean residue ellipticity ($[\Theta]_{MRE}$) was followed at 392 nm as a function of temperature and the thermodynamic parameters were also estimated by fitting the experimental data to the equation for a two-state transition of a monomer from a folded to unfolded state (Fig. 3C), as described in the previous section. The Mo-α_3DIV-L21C peptide has an estimated melting temperature of 70.4 °C and an enthalpy of unfolding of 144.4 kJ.mol^{-1}.

During the Mo-α_3DIV-L21C unfolding with the increase in temperature, the band at 392 nm decreases intensity and almost disappears at 94 °C (Fig. S2). The CD spectrum of Mo-α_3DIV-L21C in the visible region, in the presence of a reducing agent (TCEP), was acquired after the temperature ramp at room temperature (Fig. 3B) and a positive intense band at 385 nm is observed indicating that during refolding the Mo is re-incorporated into the peptide. A shift of 7 nm in the maximum wavelength is observed (from 392 to 385 nm). These results indicate that upon refolding the peptide binds Mo but there is some distortion in the metal coordination. The same experiment performed in the absence of the reducing agent produced a different result (Fig. 3D), as after the temperature ramp the CD spectrum does not present the intense band observed before the thermal unfolding.

3.3. Differential scanning calorimetry (DSC) characterization

The thermograms for the apo- and Mo-α_3DIV-L21C at pH 7.6 in the presence of TCEP are presented in Fig. 4, and its thermodynamic parameters are listed in Table 1.

The apo-α_3DIV-L21C at pH 7.6 in the presence of TCEP has a broad thermogram with a low ΔCp value that can be fitted to a one-peak transition model (T_m of 61.9 °C with a ΔH_{cal} value of 83.9 kJ.mol^{-1}). The Mo-α_3DIV-L21C peptide thermogram was fitted with a two peaks transition model. The main species has a sharper endothermic transition with a T_m of 66.1 °C and an increased enthalpy of ΔH_{cal} of 263.1 kJ mol^{-1}, and there is a second peak with an estimated T_m of 62.2 °C similar to the melting temperature of the apo-α_3DIV-L21C. The 4 °C shift observed in the melting temperature suggests that Mo insertion increases the peptide stability. The ΔH_{vH} (van't Hoff enthalpy) was determined for both apo- and Mo-α_3DIV-L21C peptide and the $\Delta H_{cal}/\Delta H_{vH}$ ratios are presented in Table 1.

The $\Delta H_{cal}/\Delta H_{vH}$ ratio for the Mo-α_3DIV-L21C peptide in the presence of TCEP is 1.5, raising the hypothesis that the unfolding is not a two-state process but may involve an intermediate. The DSC experiments performed without TCEP at the same pH gave a similar T_m value of 66.1 °C, with a significant decrease in both ΔH_{cal} and ΔH_{vH} and a higher $\Delta H_{cal}/\Delta H_{vH}$ ratio (2.3) suggesting the presence of more unfolding intermediates.

3.4. Oxidation states of Mo-α_3DIV-L21C

The visible spectrum of Mo-α_3DIV-L21C was not significantly altered

Table 1
Thermal unfolding parameters obtained by circular dichroism and differential scanning calorimetry for the apo- and Mo-α_3DIV-L21C, as well as for other apo- and holo-α_3DIVpeptides reported in the literature.

Peptide	pH	Circular Dichroism			Differential Scanning Calorimetry				Ref.
		$[\Theta]_{222nm}/[\Theta]_{208nm}$	T_m (°C)	ΔH (kJ.mol^{-1})	T_m (°C)	ΔH_{cal} (kJ.mol^{-1})	ΔH_{vH} (kJ.mol^{-1})	$\Delta H_{cal}/\Delta H_{van't\ Hoff}$	
α_3DIV-L21C[c]	7.6	1.05	60.2 [a]	112.6	61.9	83.9	86.7	0.97	this work
Mo-α_3DIV-L21C [c]	7.6	0.98	60.2 [a] 70.4 [b]	90.1 144.4	66.1	263.1	170.9	1.5	this work
Mo-α_3DIV-L21C [d]	7.6	0.97	–	–	66.1	152	66.2	2.3	this work
Fe(II)-α_3DIV-L21C [d]	8.5	1.13	61.9 [a]	143.6	–	–	–	–	[32]
α_3DIV [d]	7.0 8.2	1.03	–	–	64.4 60.2	209.2 187.9	87.2 98.9	2.4 1.9	[11]
Hg-α_3DIV [d]	8.2	1.51	–	–	84	272.4	40.7	6.7	[11]
Pb-α_3DIV [d]	8.2	1.01	–	–	83.4	247.7	55.1	4.5	[11]
Cd-α_3DIV [d]	8.2	1.07	–	–	78.1	220.5	52.5	4.2	[11]

[a] Far-UV region.
[b] Visible region.
[c] with TCEP.
[d] without TCEP.

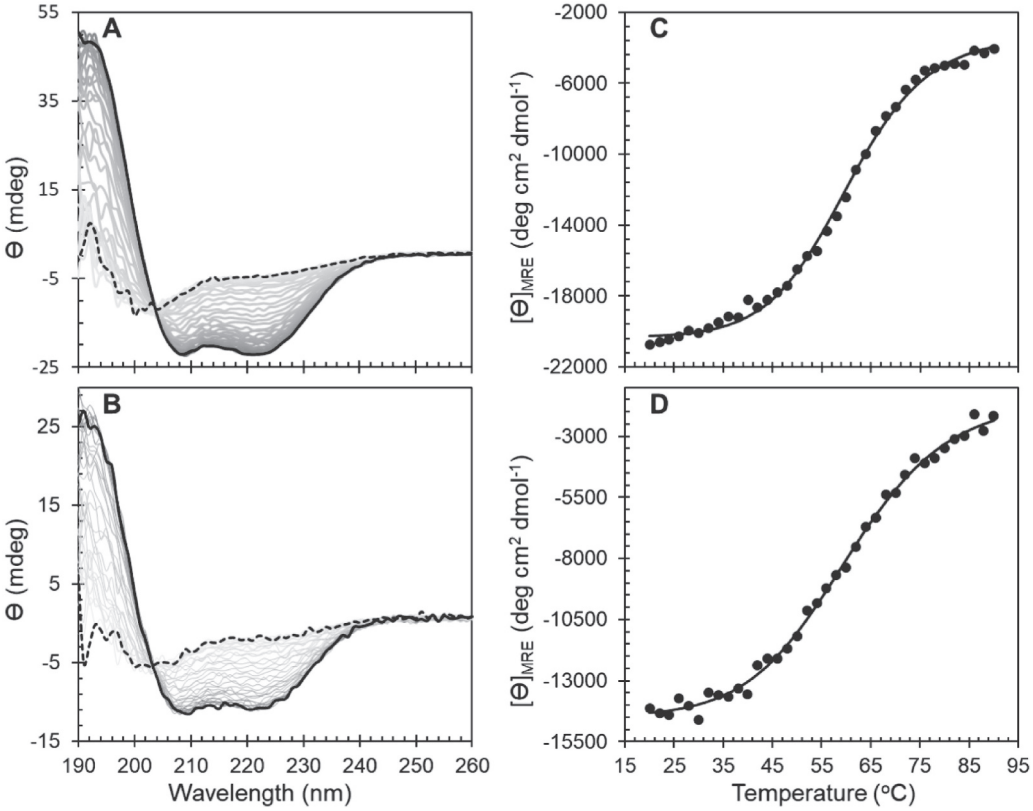

Fig. 2. Thermal stability of both apo- and Mo- α_3DIV-L21C in the presence of TCEP followed by CD in the far-UV region. A. Temperature ramp (from 10 °C to 90 °C) of the apo-α_3DIV-L21C. B. Temperature ramp (from 10 °C to 90 °C) of Mo-α_3DIV-L21C. C. and D. Mean residue ellipticity ($[\Theta]_{MRE}$) at 222 nm as a function of temperature for apo- and Mo-α3DIV-L21C, respectively. The experimental data were fitted using the equations for a two-state transition model (solid black line) [46].

by the addition of either dithionite or DTT (Fig. S3). The Mo-α_3DIV-L21C is EPR silent (data not shown) suggesting that the oxidation state of Mo is $Mo^{(VI)}$ or $Mo^{(IV)}$. After anaerobic reduction with sodium dithionite, no EPR signal was detected suggesting that no changes occurred in the oxidation state of Mo or a direct reduction from $Mo^{(VI)}$ or $Mo^{(IV)}$ occurred.

The electrochemical behaviour of the apo- and Mo-α_3DIV-L21C, in the presence of TCEP, was assessed through cyclic voltammetry comparing the apo- and the Mo-α_3DIV-L21C. A redox process was detected with a formal reduction potential, $E^{\circ\prime}$, of ~ −408 mV (Fig. 5) attributed to the peptide-coordinated Mo. The estimated number of electrons corresponding to this process is 1.2 indicating that the redox process is probably a one electron transition and favouring the hypothesis of the $Mo^{(VI)}/Mo^{(V)}$. However, one must be careful since the broad electrochemical behaviour of the process may be masking the result, and in fact two transitions may be occurring although merged $Mo^{(VI)}/Mo^{(V)}$ and $Mo^{(V)}/Mo^{(IV)}$ (Fig. S4).

4. Discussion

In this work, Mo was inserted into the apo-α_3DIV-L21C scaffold exploiting the versatility of metal-sulfide coordination that has the ability to coordinate different metal ions in biological systems [50]. In the original α_3DIV design, which contained only three cysteines, large, soft heavy metals, such as Hg(II) and Pb(II) bound to three buried cysteines stoichiometrically. Similarly, iron inserted to form Fe-α_3DIV-L21C [32] straightforwardly, however, a higher excess of Mo was needed in the incubation with the apo-peptide (1peptide:9 Mo) in order to obtain the Mo-α_3DIV-L21C. The incorporation of Mo into a more open 4-thiolate coordination scaffold, as is the case of rubredoxin where all cysteine residues are located in exposed loops, was possible by adding 2 fold molar excess of metal to the protein [30]. The requirement for such a lower molar ratio is explained by the fact that in rubredoxin the tetracysteinyl metal coordination site is more solvent exposed than in the α_3DIV-L21C scaffold (Fig. 7). In contrast, the bottom, or base, of the designed protein contains a 3-Cys site that forms a "box", which is largely sequestered from solvent. The backbone of the helices and the apolar side chains of Phe31, Ile14, and Ile63 generate the sides of the box while Phe31 serves to shelter most of the bottom of the box [51,52]. In α_3DIV, which contains only three cysteines, the top of the box was made by residues in the nonhelical loops, including Leu21. By mutating this residue to cysteine in α_3DIV-L21C, we have provided the flexibility and solvent access necessary to incorporate the molybdenum atom; however, the designed protein environment around the molybdenum is far more hydrophobic than rubredoxin. Thus, protonation of the sulfide leaving groups of TTM is likely inhibited. In addition, rubredoxin does not have as many defining structural elements when compared with the three-helix bundle of the peptide, which is a more rigid environment that may hinder the insertion of Mo (Fig. 7).

The UV–visible spectrum of Mo-α_3DIV-L21C with the two unresolved shoulders at 320 nm ($\varepsilon = 7400\ M^{-1}.cm^{-1}$) and 460 nm ($\varepsilon = 2000\ M^{-1}.cm^{-1}$) attributed to Mo-thiolate charge-transfer bands is similar to the spectra obtained for Mo-rubredoxin (shoulders at 314 nm and 450 nm) [30] (Table 2). In Mo-rubredoxin these two unresolved shoulders are shifted in the presence of DTT to 336 nm and 460 nm, due to the binding of a thiol group from DTT without changing its oxidation state (remains EPR silent). However, the Mo-α_3DIV-L21C UV–visible spectrum does not change significantly in the presence of DTT suggesting that DTT is neither reducing nor coordinating the Mo atom. The latter point is fully consistent with the hydrophobic box surrounding the molybdenum and protecting it from exogenous ligands in the designed system. The oxidation state of Mo in both Mo-rubredoxin and DTT treated Mo-rubredoxin is Mo(VI). The UV–visible spectra of Mo-α_3DIV-L21C does not suggest that the Mo in the peptide is in a different oxidation state

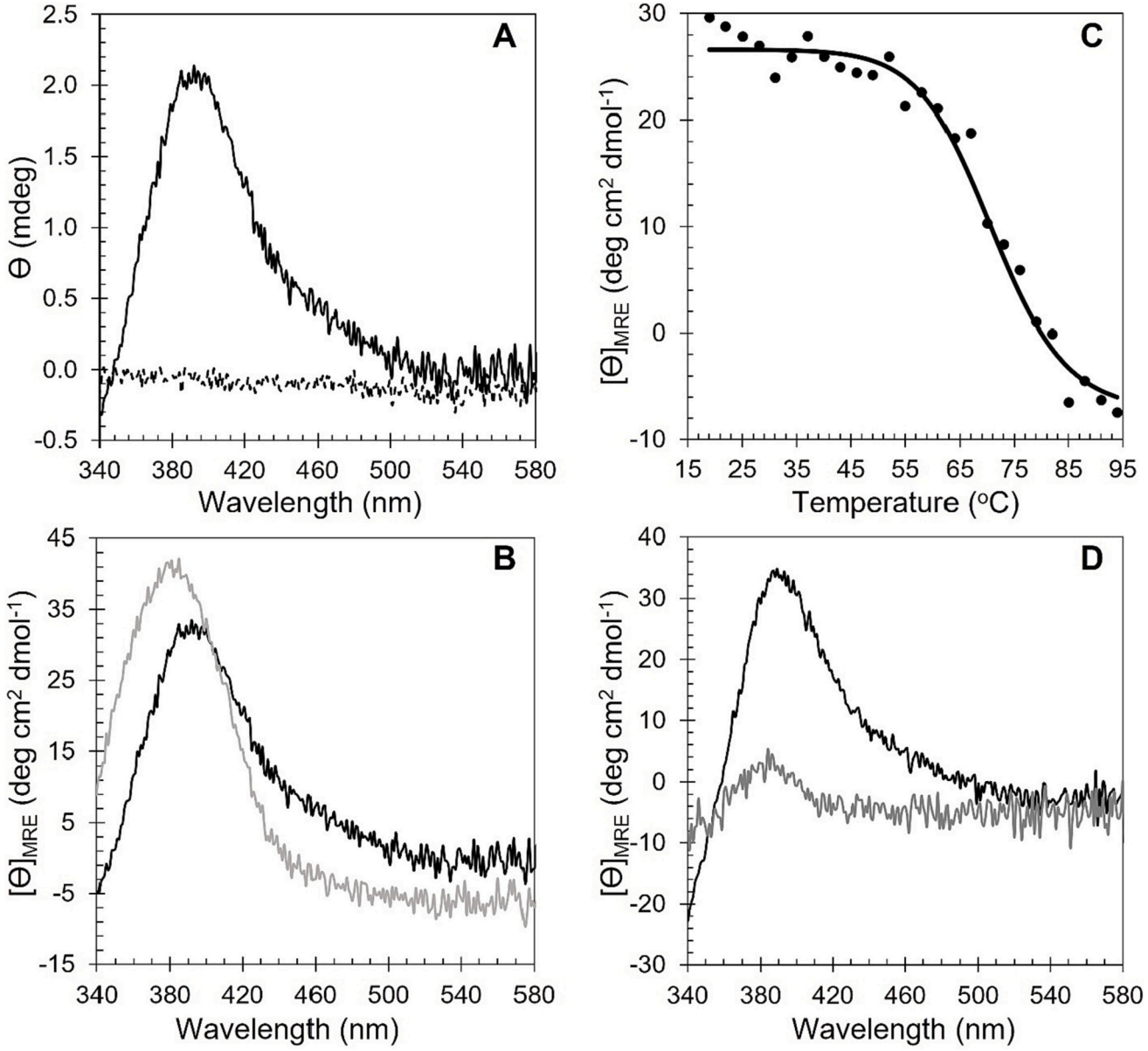

Fig. 3. Circular dichroism spectra in the visible region of Mo-α_3DIV-L21C. **A.** Dark line - Mo-α_3DIV-L21C in the presence of TCEP; dashed line - TTM. **B.** Dark line - Mo-α_3DIV-L21C at 25 °C before the temperature ramp, gray line - Mo-α_3DIV-L21C at 25 °C after the temperature ramp (20 to 94 °C) in the presence of TCEP. **C.** Mean residue ellipticity ($[\Theta]_{MRE}$) at 222 nm as a function of temperature for the Mo-α_3DIV-L21C peptide in the presence of TCEP. **D.** Dark line - Mo-α_3DIV-L21C at 25 °C before the temperature ramp; gray line - Mo-α_3DIV-L21C at 25 °C after the temperature ramp (20 to 94 °C) in the absence of TCEP.

than Mo(VI).

CD studies in the far-UV region of both apo- and Mo-α_3DIV-L21C show typical CD spectra of well folded α-helical structures with no significant structural changes upon Mo binding other than a small decrease in helicity. The decrease in helicity can be explained by the perturbation caused by the binding of Mo to the cysteine residues, as previously observed for Hg(II), Pb(II), or Cd(II) bound to α_3DIV [11,51].

Thermal stability studies were performed using CD in the far-UV region following changes in the secondary structure elements of apo- and Mo-α_3DIV-L21C in the presence of TCEP. The T_m values are the same (60.2 °C) suggesting that Mo insertion does not disrupt the α_3DIV-L21C secondary structure but does not provide further stability to this structural level, on the contrary, a small decrease in the unfolding enthalpy is observed (Table 1). However, when the CD thermal studies follow the Mo signal in the visible region (at 392 nm) the T_m is 70.4 °C showing that the Mo binding site surroundings are more stable and the enthalpy of unfolding increases significantly. DSC studies provide information on the overall unfolding process and a T_m of 61.9 °C was obtained for the apo-α_3DIV-L21C and 66.1 °C for Mo-α_3DIV-L21C representing an increase of ~4 °C in the melting temperature for the metallated scaffold and an increase of 179.2 kJ.mol^{-1} in the calculated unfolding enthalpy. The stability enhancement provided by Mo insertion in α_3DIV-L21C shows that the Mo—S bonds formed are supplementing other bonds essential to the peptide folding, such as hydrophobic interactions, salt-bridges, or hydrogen bonds. The two different values of melting temperature obtained in CD analysis and the intermediated melting temperature obtained by DSC suggest that the secondary structure undergoes an initial thermal-induced denaturation prior to the loss of the molybdenum-thiolate coordination, reinforcing the strength of the Mo—S bonds.

Furthermore, the replacement of a Leu residue by a Cys to form the tetrathiolate metal-binding site in the α_3DIV scaffold decreases the potential for hydrophobic interactions but increases the stabilization by the formation of disulphide bonds in the absence of a reducing agent and

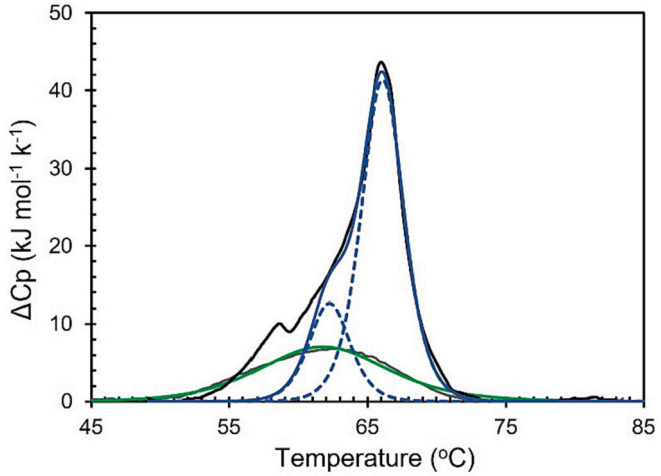

Fig. 4. Thermograms of apo-α_3DIV-L21C (gray line) and Mo-α_3DIV-L21C peptide (black line) at pH 7.6, fitted to a one-peak transition model (green) and two-peak transition model (blue line is the sum of the two dash lines correspondent to the two transitions), respectively. (For interpretation of the references to colour in this figure legend, the reader is referred to the web version of this article.)

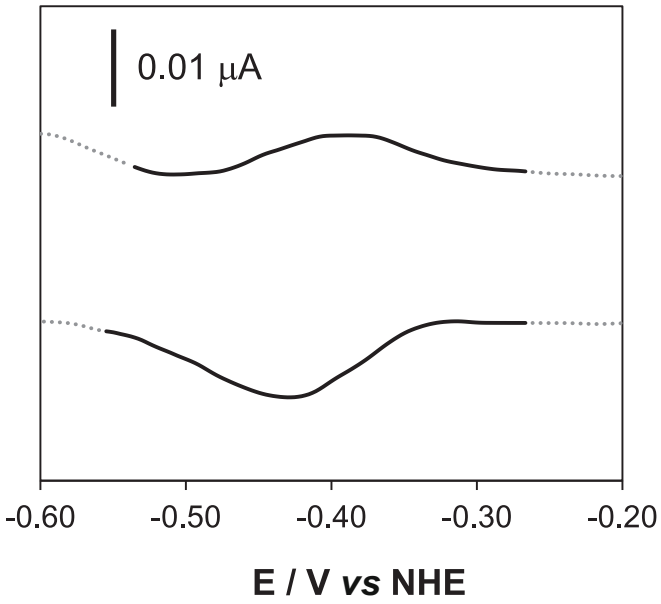

Fig. 5. Representative cyclic voltammogram of the Mo-α_3DIV-L21C, at the potential region of interest (after normalization and subtraction of the apo-α_3DIV-L21C cyclic voltammogram); experimental conditions: ν = 20 mV.s^{-1}; E_{oc} = +0.04 V. The complete voltammogram with the extended potential window between +0.4 to −0.66 V is presented in Fig. S4.

metal ion. DSC studies of apo-α_3DIV-L21C in the absence of a reducing agent gave almost no signal (data not shown) probably due to the existence of several conformations coming from different disulphide bonds formed in the peptide, which gave rise to the observation of a very broad transition. The T_m of Mo-α_3DIV-L21C is the same in the presence or absence of TCEP but the enthalpy increases 1.7-fold with TCEP indicating that the Mo—S bonds formed do stabilize the peptide when compared with the S—S bonds that are formed in the denaturation process in the absence of reducing agent.

The observed redox couple formal potential value of $E^{\circ\prime} = -408$ mV *vs.* NHE although slightly more positive, is in agreement with the reduction potential determined for the Mo-substituted rubredoxin ($E^{\circ\prime}$ = −493 mV *vs.* NHE) [30]. The formal reduction potential combined with the EPR silent state observed suggest that the Mo-peptide is mainly in the $Mo^{(VI)}$ oxidation. Sodium dithionite addition did not result in changes in the EPR silent state or significantly changed the UV–visible spectrum suggesting that dithionite was not able to reduce the Mo center of the Mo-α_3DIV-L21C peptide, whereas in Mo-rubredoxin dithionite could reduce $Mo^{(VI)}$ to $Mo^{(V)}$ and $Mo^{(IV)}$ [30]. In the conditions used in this experiment the theoretical potential of sodium dithionite at pH 7.6 for concentrations closer to the ones used by us, without mediators, is approximately −520 mV [54] with a difference of −110 mV between the potential of sodium dithionite compared to Mo-α3DIV-L21C (−408 mV). This difference in potential should be enough to observe reduction (at least to some extension) but probably the hydrophobic environment around the Mo center discussed above, hindered the process. This could result in a slow reduction kinetics that is not favoured by electrostatic interactions between the reducer and the Mo. Besides there are a few examples of metalloproteins that cannot be fully or at all reduced by sodium dithionite and the reasons cannot be explained by the redox potential of dithionite. [55–57]

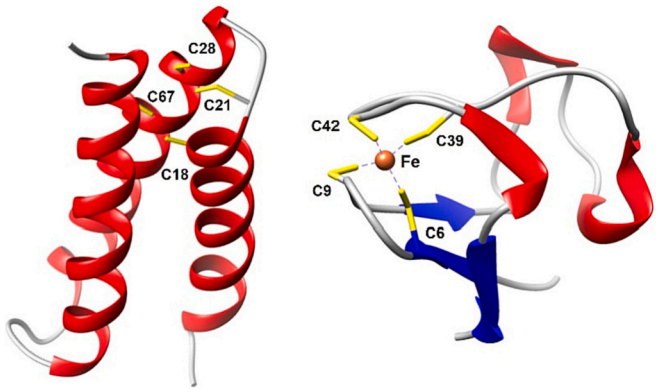

Fig. 7. Comparison of the three-dimensional structure of (a) apo-α_3DIV-L21C scaffold and (b) rubredoxin from *D. gigas* (PDB: 2DSX), highlighting their different secondary structure composition between α-helices highlighted in red; β-sheets in blue and loops in gray. Structures were visualized with Chimera 1.11. (For interpretation of the references to colour in this figure legend, the reader is referred to the web version of this article.)

Table 2
Characteristic charge-transfer bands of Mo-α_3DIV-L21C peptide, Mo-rubredoxin, DTT-treated Mo-rubredoxin, Mo-rubredoxin, and TTM compound [30,53].

Mo-α_3DIV-L21C	Mo-rubredoxin	Mo-rubredoxin (DTT)	TTM compound
320 nm (ε = 7400 M^{-1}. cm^{-1})	**314 nm** (ε = 8010 M^{-1}. cm^{-1})	**336 nm** (ε = 7760 M^{-1}. cm^{-1})	**318 nm** (ε = 17,600 M^{-1}. cm^{-1})
460 nm (ε = 2000 M^{-1}. cm^{-1})	**450 nm** (ε = 1020 M^{-1}. cm^{-1})	**460 nm** (ε = 1910 M^{-1}. cm^{-1})	**469 nm** (ε = 12,400 M^{-1}. cm^{-1})

The electrochemical results do not rule out that a small fraction of the Mo-α_3DIV-L21C may be initially in a more reduced oxidation state, probably $Mo^{(IV)}$. This could be explained by a partial loss of one of the four thiol groups that is coordinating the Mo atom, that could stabilize Mo in the $Mo^{(IV)}$ oxidation state as observed previously by EXAFs for HMCS-CT [58], a member of the molybdenum cofactor (Moco) sulfurase C-terminal (MOSC) domain superfamily of pyranopterin molybdenum (Mo) proteins. In the future this hypothesis needs to be corroborated by resonance Raman and EXAFS studies.

5. Conclusions

The incorporation of a Mo within the tetracysteinyl binding-site of

the α_3DIV-L21C scaffold was proven by different approaches and it is an interesting candidate as a structural model for the Mo-*bis* MGD enzymes. The incorporation ratio of 1 peptide:1 Mo was proven by metal analysis and by the observation of S—Mo charge-transfer bands in the UV–visible spectrum and the appearance of a positive absorption band in the CD visible region at 392 nm. The absorption bands relate to the bands observed for Mo-rubredoxin and the incorporation of Mo thermostabilized the α_3DIV-L21C scaffold, as shown by CD in the visible region and DSC.

We favor a $Mo^{(VI)}$ oxidation state due to the EPR silent signal and the formal redox potential of −408 mV *vs.* NHE that is quite similar to the one of Mo-rubredoxin. The inability to reduce Mo-α_3DIV-L21C adding reducing agents, always observing an EPR silent signal and almost no changes in the UV–visible spectra, can be explained by the lower solvent accessibility due to the hydrophobic environment surrounding the Mo-site associated with the low formal potential of the Mo center and structural rigidity imposed by the three helix-bundle.

Declaration of Competing Interest

The authors declare that they have no known competing financial interests or personal relationships that could have appeared to influence the work reported in this paper.

The authors declare the following financial interests/personal relationships which may be considered as potential competing interests:

Data availability

Data will be made available on request.

Acknowledgements

This work was supported by Fundação para a Ciência e Tecnologia, I. P. (FCT) through project grants to JJGM (PTDC/BTA-BTA/0935/2020) and SRP (PTDC/BIA-BQM/29442/2017). PB would thank the PTNMRPhD (PD/00065/2013) This work was also supported by national funds from FCT in the scope of the project Associate Laboratory for Green Chemistry-LAQV, (FCT/MCTES; UIDB/50006/2020, UIDP/50006/2020 and LA/P/0008/2020) and UIDP/04378/2020 and UIDB/04378/2020 of the Research Unit on Applied Molecular Biosciences - UCIBIO and the project LA/P/0140/2020 of the Associate Laboratory Institute for Health and Bioeconomy - i4HB. VLP thanks the NIH for support (GM141086).

Appendix A. Supplementary data

Supplementary data to this article can be found online at https://doi.org/10.1016/j.jinorgbio.2022.112096.

References

[1] V. Nanda, R.L. Koder, Nat. Chem. 2 (2010) 15–24.
[2] V. Sharma, M. Bachwani, Curr. Enzym. Inhib. 7 (2011) 178–189.
[3] R. Breslow, Science 218 (1982) 532–537.
[4] Y. Murakami, J.I. Kikuchi Ji, Y. Hisaeda, O. Hayashida, Chem. Rev. 96 (1996) 721–758.
[5] L. Regan, Curr. Opin. Biotechnol. 2 (1991) 544–550.
[6] W.B. Motherwell, M.J. Bingham, Y. Six, Tetrahedron 57 (2001) 4663–4686.
[7] F. Yu, V.M. Cangelosi, M.L. Zastrow, M. Tegoni, J.S. Plegaria, A.G. Tebo, C. S. Mocny, L. Ruckthong, H. Qayyum, V.L. Pecoraro, Chem. Rev. 114 (2014) 3495–3578.
[8] B.K. Maiti, R.M. Almeida, I. Moura, J.J.G. Moura, Coord. Chem. Rev. 352 (2017) 379–397.
[9] K. Koebke, T.B.J. Pinter, W.C. Pitts, V.L. Pecoraro, Chem. Rev. 122 (2022) 12046–12109.
[10] A.J. Doerr, G.L. McLendon, Inorg. Chem. 43 (2004) 7916–7925.
[11] J.S. Plegaria, V.L. Pecoraro, Israel J. Chem. 55 (2015) 85–95.
[12] A.F. Peacock, Curr. Opin. Chem. Biol. 17 (2013) 934–939.
[13] M.L. Zastrow, V.L. Pecoraro, Coord. Chem. Rev. 257 (2013) 2565–2588.
[14] L. Baltzer, H. Nilsson, J. Nilsson, Chem. Rev. 101 (2001) 3153–3163.
[15] S.R. Pauleta, M. Carepo, R. Grazina, I. Moura, J.J.G. Moura, in: V. Pecoraro, Z. Guo (Eds.), Comprehensive Inorganic Chemistry III from Biology to Nanotechnology vol. 2, Elsevier Ltd, Amsterdam, 2023 (in Press).
[16] I. Moura, A.S. Pereira, P. Tavares, J.J.G. Moura, Adv. Inorg. Chem. 47 (1999) 361–419.
[17] L.C. Sieker, R.E. Stenkamp, J. LeGall, Methods Enzymol. 243 (1994) 203–216.
[18] P.M. Vignais, B. Billoud, Chem. Rev. 107 (2007) 4206–4272.
[19] R. Cammack, Nature 397 (1999) 214–215.
[20] A.C. Rosenzweig, Chem. Biol. 9 (2002) 673–677.
[21] M.D. Harrison, C.E. Jones, C.T. Dameron, J. Biol. Inorg. Chem. 4 (1999) 145–153.
[22] J.M. Tunney, J. McMaster, C.D. Garner, in: A.J. McCleverty, T.J. Meyer (Eds.), Comprehensive Coordination Chemistry II vol. 8, Elsevier Ltd, Amsterdam, 2004, pp. 459–477.
[23] V.V. Vrajmasu, E.L. Bominaar, J. Meyer, E. Munck, Inorg. Chem. 41 (2002) 6358–6371.
[24] M. Maher, M. Cross, M.C. Wilce, J.M. Guss, A.G. Wedd, Acta Crystallogr. D Biol. Crystallogr. 60 (2004) 298–303.
[25] J.W. Slater, S.C. Marguet, H.A. Monaco, H.S. Shafaat, J. Am. Chem. Soc. 140 (2018) 10250–10262.
[26] B.K. Maiti, L.B. Maia, A.J. Moro, J.C. Lima, C.M. Cordas, I. Moura, J.J.G. Moura, Inorg. Chem. 57 (2018) 8078–8088.
[27] Z. Dauter, K.S. Wilson, L.C. Sieker, J.M. Moulis, J. Meyer, Proc. Natl. Acad. Sci. U. S. A. 93 (1996) 8836–8840.
[28] M. Archer, A.L. Carvalho, S. Teixeira, I. Moura, J.J. Moura, F. Rusnak, M.J. Romão, Protein Sci. 8 (1999) 1536–1545.
[29] D.M. LeMaster, M. Minnich, P.J. Parsons, J.S. Anderson, G. Hernandez, J. Inorg. Biochem. 100 (2006) 1410–1412.
[30] B.K. Maiti, L.B. Maia, C.M. Silveira, S. Todorovic, C. Carreira, M.S. Carepo, R. Grazina, I. Moura, S.R. Pauleta, J.J. Moura, J. Biol. Inorg. Chem. 20 (2015) 821–829.
[31] T. Conrads, C. Hemann, G.N. George, I.J. Pickering, R.C. Prince, R. Hille, J. Am. Chem. Soc. 124 (2002) 11276–11277.
[32] A.G. Tebo, T.B.J. Pinter, R. Garcia-Serres, A.L. Speelman, C. Tard, O. Seneque, G. Blondin, J.M. Latour, J. Penner-Hahn, N. Lehnert, V.L. Pecoraro, Biochemistry 57 (2018) 2308–2316.
[33] A.G. Tebo, A. Quaranta, V.L. Pecoraro, A. Aukuloo, ChemPhotoChem 5 (2021) 665–668.
[34] A.G. Tebo, L. Hemmingsen, V.L. Pecoraro, Metallomics 7 (2015) 1555–1561.
[35] C.J. Henehan, D.L. Pountney, O. Zerbe, M. Vasák, Protein Sci. 2 (1993) 1756–1764.
[36] Z. Xiao, M.J. Lavery, M. Ayhan, S.D.B. Scrofani, M.C.J. Wilce, J.M. Guss, P. A. Tregloan, G.N. George, A.G. Wedd, J. Am. Chem. Soc. 120 (1998) 4135–4150.
[37] A.G. Tebo, L. Hemmingsen, V.L. Pecoraro, Metallomics 7 (2015) 1555–1561.
[38] A. Waterhouse, M. Bertoni, S. Bienert, G. Studer, G. Tauriello, R. Gumienny, F. T. Heer, T.A.P. de Beer, C. Rempfer, L. Bordoli, R. Lepore, T. Schwede, Nucleic Acids Res. 46 (W1) (2018) W296–W303.
[39] F.F. Pettersen, T.D. Goddard, C.C. Huang, G.S. Couch, D.M. Greenblatt, E.C. Meng, T.E. Ferrin, J. Comput. Chem. 25 (2004) 1605–1612.
[40] O.H. Lowry, N.J. Rosebrough, A.L. Farr, R.J. Randall, J. Biol. Chem. 193 (1951) 265–275.
[41] S.M. Kelly, T.J. Jess, N.C. Price, Biochim. Biophys. Acta 1751 (2005) 119–139.
[42] S.M. Kelly, N.C. Price, Curr. Protein Pept. Sci. 1 (2000) 349–384.
[43] L. Whitmore, B.A. Wallace, Biopolymers 89 (2008) 392–400.
[44] R.W. Woody, A.K. Dunker, in: G. Fasman (Ed.), Circular Dichroism and the Conformational Analysis of Biomolecules vol. 4, Springer, Boston, MA, New York, 1996, pp. 109–157.
[45] N.J. Greenfield, TrAC Trends Anal. Chem. 18 (1999) 236–244.
[46] N.J. Greenfield, Nat. Protoc. 1 (2006) 2527–2535.
[47] L.B. Anderson, C.N. Reilley, J. Electroanal. Chem. 10 (1965) 295–305.
[48] C. Leger, P. Bertrand, Chem. Rev. 108 (2008) 2379–2438.
[49] C.M. Cordas, M. Campanico, R. Baptista, L.B. Maia, I. Moura, J.J.G. Moura, J. Inorg. Biochem. 196 (2019), 110694.
[50] B.K. Maiti, L.B. Maia, J.J.G. Moura, J. Inorg. Biochem. 227 (2022), 111687.
[51] J.S. Plegaria, S.P. Dzul, E.R. Zuiderweg, T.L. Stemmler, V.L. Pecoraro, Biochemistry 54 (2015) 2858–2873.
[52] S. Chakraborty, J.Y. Kravitz, P.W. Thulstrup, L. Hemmingsen, W.F. DeGrado, V. L. Pecoraro, Angew. Chem. Int. Ed. 50 (2011) 2049–2053.
[53] S.H. Laurie, Eur. J. Inorg. Chem. 2000 (2000) 2443.
[54] S.G. Mayhew, Eur. J. Biochem. 85 (1978) 535–547.
[55] C.M. Cordas, A.G. Duarte, J.J.G. Moura, I. Moura, Biochim. Biophys. Acta 1827 (2013) 233–238.
[56] S.R. Pauleta, M.S.P. Carepo, I. Moura, in: A. Sigel, E. Freisinger, R.K.O. Sigel (Eds.), Transition Metals and Sulfur – A Strong Relationship for Life: Metal Ions in Life Sciences vol. 20, Springer, Germany, 2020, pp. 139–164.
[57] S.R. Pauleta, M.S.P. Carepo, I. Moura, Coord. Chem. Rev. 387 (2019) 436–449.
[58] L.J. Giles, C. Ruppelt, J. Yang, R.R. Mendel, F. Bittner, M.L. Kirk, Inorg. Chem. 53 (2014) 9460–9462.